AGU PUBLICATIONS

Water Resources Research

RESEARCH ARTICLE
10.1002/2013WR014516

Special Section:
Patterns in Soil-Vegetation-Atmosphere Systems: Monitoring, Modelling and Data Assimilation

Spatiotemporal relations between water budget components and soil water content in a forested tributary catchment

Alexander Graf[1], Heye R. Bogena[1], Clemens Drüe[2], Horst Hardelauf[1], Thomas Pütz[1], Günther Heinemann[2], and Harry Vereecken[1]

[1]Agrosphere Institute, Forschungszentrum Jülich, Jülich, Germany, [2]Umweltmeteorologie, Universität Trier, Trier, Germany

Abstract We examined 3 years of measured daily values of all major water budget components (precipitation *P*, potential evapotranspiration *PET*, actual evapotranspiration *ET*, and runoff *R*) and volumetric soil water content θ of a small, forested catchment located in the west of Germany. The spatial distribution of θ was determined from a wireless sensor network of 109 points with 3 measurement depths each; *ET* was calculated from eddy-covariance tower measurements. The water budget was dominantly energy limited, with *ET* amounting to approximately 90% of *PET*, and a runoff ratio *R/P* of 56%. *P*, *ET*, and *R* closed the long-term water budget with a residual of 2% of precipitation. On the daily time scale, the residual of the water budget was larger than on the annual time scale, and explained to a moderate extent by θ ($R^2 = 0.40$). Wavelet analysis revealed subweekly time scales, presumably dominated by unaccounted fast-turnover storage terms such as interception, as a major source of uncertainty in water balance closure. At weekly resolution, soil water content explained more than half ($R^2 = 0.62$) of the residual. By means of combined empirical orthogonal function and cluster analysis, two slightly different spatial patterns of θ could be identified that were associated with mean θ values below and above 0.35 cm^3/cm^3, respectively. The timing of these patterns as well as the varying coherence between *PET*, *ET*, and soil water content responded to changes in water availability, including a moderate response to the European drought in spring 2011.

Key Points:
- Water budget and distributed soil water content of small catchment analyzed
- Budget closed on annual basis, short-term residual correlated with water content
- EOF analysis reveals two patterns, hysteresis relation to mean water content

Correspondence to:
A. Graf,
a.graf@fz-juelich.de

Citation:
Graf, A., H. R. Bogena, C. Drüe, H. Hardelauf, T. Pütz, G. Heinemann, and H. Vereecken (2014), Spatiotemporal relations between water budget components and soil water content in a forested tributary catchment, *Water Resour. Res.*, *50*, 4837–4857, doi:10.1002/2013WR014516.

Received 2 AUG 2013
Accepted 27 MAY 2014
Accepted article online 30 MAY 2014
Published online 12 JUN 2014

1. Introduction

Improvement of our understanding of spatiotemporal dynamics of hydrological fluxes at the catchment scale is frequently restricted by lack of data. While modeling approaches allow to predict and understand sensitivities of such dynamics [e.g., *Albertson and Montaldo*, 2003], models cannot be applied to real-world catchments without additional assumptions. In particular, distributed modeling suffers from lack of knowledge on the spatial distribution of key parameters such as soil hydraulic parameters or root water uptake. Due to increased monitoring capabilities, data sets with high temporal and spatial resolution of fluxes and states are becoming more and more available, opening new possibilities for data-driven investigation approaches. Recently, four long-term observatories have been established in Germany as part of the TERENO project (http://teodoor.icg.kfa-juelich.de). Among other parameters, hydrological phenomena are observed at scales from small highly instrumented headwater catchments to mesoscale watersheds covering several 1000 km^2 [*Zacharias et al.*, 2011; *Bogena et al.*, 2012]. At the headwater catchment scale, experiments are conducted in which global change effects on terrestrial systems are investigated using controlled manipulation, e.g., sheltering and temperature increase (www.ufz.de/exploratories/index.php?en=21240), lysimeter translocation [*Pütz et al.*, 2011], and deforestation [*Bogena et al.*, 2014]. Field experiments are also being used to provide valuable data sets for the development and evaluation of hydrological models [*Cornelissen et al.*, 2014] and to understand the magnitude of measurement errors [*Kampf and Burges*, 2010]. With state of the art monitoring methods, the major water budget components evapotranspiration (*ET*), precipitation (*P*), and runoff (*R*) as well as the spatial distribution of soil water storage (θ) have been assessed in the TERENO test site Wüstebach (see section 2.3) for a period of 3 years. This comprehensive hydrological data set offers the opportunity for a data-driven investigation of the spatiotemporal pattern of hydrological fluxes and states without the need to make detailed assumptions on involved processes. At the same time, it serves as a characterization of the hydrological catchment state prior to a deforestation in late summer 2013 [*Bogena et al.*, 2014].

Here, we present a detailed overview of the hydrological state of the catchment along with a methodological framework for the empirical characterization of the involved processes. Our research questions are, in

order of increasing detail: (1) Is it possible to close the long-term catchment water balance using state of the art monitoring data (including measured actual *ET*)? (2) Can distributed soil water content measurements within the catchment be used as a proxy for the storage term, and thus explain the residual of the balance on subannual time scales? (3) For which conditions and time scales are further storage terms most important and need to be considered in water balance analyses? (4) Are observed variations in soil water storage a mere result of the varying average and variance parameters of a single pattern? If not, can those variations in the pattern which go beyond variations of the spatial average and standard deviation of soil water content be systematically related to them?

In order to answer these questions, methods are needed to efficiently describe pattern variations over time, and to inspect correlations between two variables as a function of time and frequency. For the first task, we chose the empirical orthogonal function (EOF) concept because it is able to describe recurring pattern variations beyond mere average and variance changes as time series of only a few (in our case two) variables. For the second task, we chose the wavelet coherence analysis because it provides a continuous time, frequency, and phase lag specification of the global correlation between two variables. Both analysis techniques avoid prior assumptions on the identity of the relevant time scales (continuous wavelet analysis) or patterns (EOF), thus minimizing the risk of overlooking unexpected processes. By identifying the most relevant time scales or patterns, they can often guide the way to a simpler method, as is demonstrated later in this paper.

Wavelet analysis is a time series analysis technique that overcomes some of the problems associated with more basic techniques such as Fourier analysis, in particular with respect to nonstationarity (section 2.8). Of particular interest for our research questions is the resulting property that variances and covariances can be described as a function of both time and frequency. For variances (univariate case), the superiority of wavelet analysis on nonstationary runoff and groundwater level data has been demonstrated by *Kang and Lin* [2007]. If applied to two variables which were observed simultaneously, the wavelet transform can be used to quantify their correlation (wavelet coherence analysis) [*Torrence and Compo*, 1998] separately for each point in the time and frequency domain. The applicability of wavelet coherence analysis to hydrology has been demonstrated by *Lauzon et al*. [2004] and *Parent et al*. [2006]. *Lauzon et al*. [2004] applied wavelet coherence analysis to time series of precipitation, soil moisture and runoff in order to unveil the role of seasonal changes in the response of runoff to precipitation, and of soil water as a mediator in the otherwise poor relation between precipitation and runoff. The highest correlation of soil water content to both, precipitation and runoff, was found for water content measured at intermediate depths (35 cm). Shallower measurements correlated best with short-term changes in precipitation, deeper measurements with the seasonal cycle of runoff. Here, we use wavelet coherence analysis to investigate the correlation between soil water content at three different depths and the water balance, in particular its allocation to certain times or frequencies.

While the wavelet transform can also be used in space instead of time, if a regular data grid is available, it cannot be applied directly to data from irregular sensor networks. The time series of each single sensor can be fed into wavelet analysis, but for large networks the computational effort is huge. In addition, the results will become highly redundant and difficult to interpret. The most important part of information from multiple sensors can be described by the time series of the spatial average and the spatial standard deviation, but at the cost of losing information on the actual pattern [*Western et al*., 2002].

On a data set covering small spatial and temporal scales of up to 90 m and 2 months, *Parent et al*. [2006] used principal component analysis to reduce the information from seven soil water content measurements. In this way, information describing not only the average and variance but also the evolution of the actual pattern can be fed into wavelet analysis as one or few additional time series. While the number of variables to wavelet transform and thus the computational effort is largely reduced, principal component analysis ensures that the few remaining significant variables still describe most of the total variance. In several studies on spatial soil water content or soil respiration data sets without reference to wavelet analysis, it was shown that the first two principal components explain half or more of total variance and exhibit a clearer spatial dependence, enhancing interpolation [*Perry and Niemann*, 2007, 2008; *Korres et al*., 2010; *Graf et al*., 2012]. In such spatial contexts, principal component analysis is also known as EOF analysis; it can be performed with focus on temporal (transforming the original time series into orthogonal new time series) or on spatial (transforming the original maps into orthogonal new maps) variability.

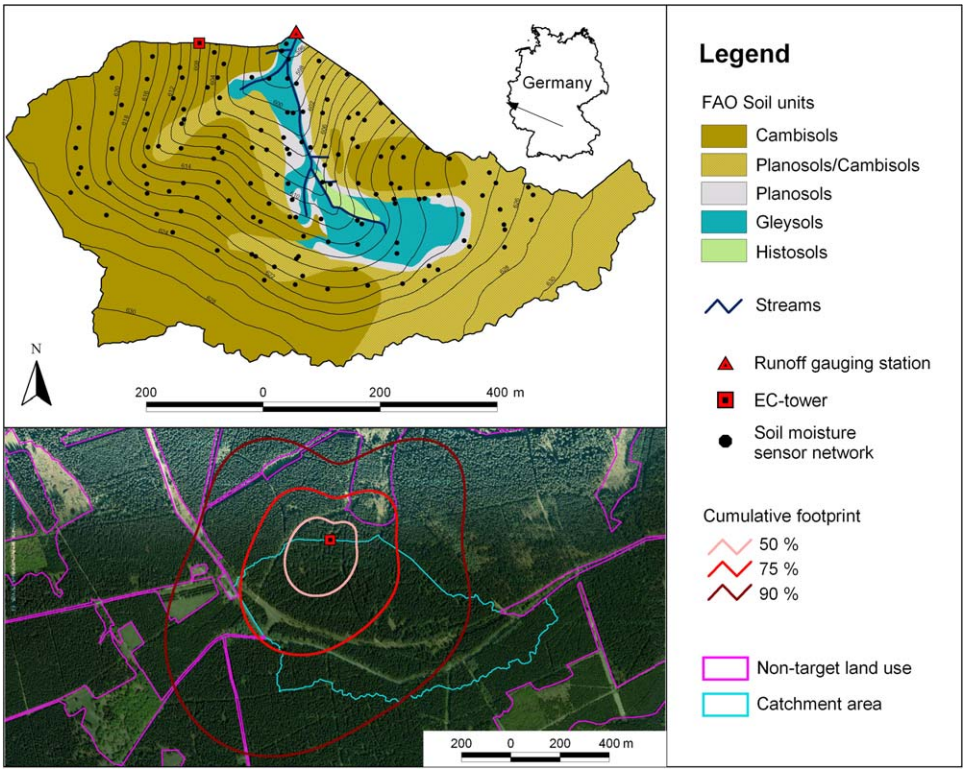

Figure 1. Soil map of the 38.520 ha Wüstebach catchment area and the hydro-meteorological instrumentation used for this study. (bottom) Cumulative footprint of the eddy-covariance (EC) tower over the study period. The map of nontarget areas continues over a larger area (section 3); where it indicates a nontarget area despite apparent spruce forest, clear-cuts or windthrows occurred between the date of the aerial view (2007) and the end of the study period.

Here, we used an approach similar to *Parent et al*. [2006] but focused on spatial variability to reduce the information content of a large sensor network to time series of mean, variance, and loadings of the two most important spatial patterns. Subsequently, we feed the obtained time series into the wavelet coherence analysis. To our knowledge, this particular combination of both methods has not yet been applied to a long-term water balance data set at the catchment scale.

2. Material and Methods

2.1. Study Site

Our study focuses on a 38.52 ha small, forested subcatchment of the Rur catchment in the westernmost part of Germany. The Wüstebach catchment (50°30′N, 06°19′E, Figure 1) near the Belgian border is one of the intensive study sites of TERENO [*Zacharias et al*., 2011]. Altitude ranges from 595 to 629 m a.s.l., slopes are 3.6% on average and up to 10.4%. The bedrock, at depths of 1–2 m below the surface, is fractured Devonian shale and Sandstone of low porosity and low hydraulic conductivity [*HK100*, 2009]. Soils are shallow with an average depth of 1.6 m and the most important soil texture is silty clay loam. Cambisols and Planosols are mainly located on hillslopes, whereas Gleysols or half-bogs are located in the riparian zone. More than 90% of the forest is comprised of spruce (*Picea abies*) trees planted in 1946 [*Etmann*, 2009], with a typical canopy height of about 25 m. Since the catchment is part of the newly founded National Park "Eifel," subdomains with a slow expected succession toward natural (deciduous) vegetation are scheduled for complete or partial cutting, beginning in summer 2013. In order to monitor the energy and matter balance changes associated with this procedure, various continuously logging instruments were set up between 2008 and 2010, including a wireless soil water content sensor network and an eddy-covariance tower. Here, we will use only hydrological variables from the 3 year study period 1 May 2010 to 30 April 2013, which is characterized by an almost continuous availability of all required variables and ends with the preparations

for the first deforestation. Acquisition and preprocessing of the variables of interest is described in the following subsections, concluding with a description of the empirical orthogonal function and the wavelet coherence methodology, which will be used to explore relations between these variables. Although some variables are preprocessed on a half-hourly or hourly basis for accurate determination and gap-filling, the final analysis is based on daily averages and sums.

2.2. Precipitation *P*

Because precipitation time series and sums are highly sensitive to measurement methodology and the gap-filling of data acquisition gaps is delicate, we relied on precipitation time series from the nearest-by official meteorological station Kalterherberg (German Weather Service, DWD), which is located 8 km to the west at 535 m a.s.l. The rain gauge was heated for a delayless and complete determination of the snow water equivalent. Systematic underestimations due to wind field distortion and funnel evaporation were corrected according to the estimation procedure by *Richter* [1995] which is used as a standard by the DWD. This procedure adds a correction term $\Delta P = bP^{\varepsilon}$ to each daily sum of raw measured precipitation P. The empirical parameters b and ε are given separately for four precipitation types (summer and winter rainfall, pure snow and mixed precipitation) and, in case of b, also for four classes of differently sheltered terrain position, which are specified by the mean horizon elevation angle (2°, 5°, 9.5°, 16°). The importance of the correction in annual sums typically varies between 7% and 15% [*Richter*, 1995], with low horizon elevations typically resulting in higher corrections because of the stronger effect of wind field distortion around the gauge in less sheltered situations. The original procedure of the DWD, defines daily sums from 6:00 local time to 6:00 of the next day for historical reasons. We replicated the methodology aggregating the hourly values to true daily sums (0:00–0:00), using the same horizon elevation angle (16°) but only three precipitation types for summer rainfall (May through September), winter rainfall, and snow (days with an average temperature <0°C), respectively. When applied to the 6:00 based day definition, our results matched those of the DWD closely (R^2 and regression slope unity to three digits, bias 1.1 mm per annum).

2.3. Potential Evapotranspiration *PET*

Potential grass reference evapotranspiration *PET* was calculated according to *Allen et al*. [1998], using the scheme for hourly data

$$\lambda \cdot PET = \frac{\Delta(R_n - G) + \rho c_p \frac{e_s - e}{r_a}}{\Delta + \gamma\left(1 + \frac{r_s}{r_a}\right)}, \tag{1}$$

where λ is the latent heat of vaporization (2.45×10^6 J kg^{-1}), $\Delta =$ the slope of the saturation vapor pressure curve over temperature (Pa K^{-1}), $R_n - G$ the net radiation minus ground heat flux (W m^{-2}), ρ the air density (kg m^{-3}), c_p the specific heat capacity of air at constant pressure (1.013×10^3 J K^{-1} kg^{-1}), $e_s - e$ the vapor pressure deficit (Pa), γ the psychrometric constant (Pa K^{-1}), and r_a and r_s the aerodynamic and stomatal resistance of a well-watered reference grass surface, respectively (s m^{-1}). The computation of r_a, r_s, ρ, γ, e_s, and Δ from weather station data followed equations (4) and (5), Box 6, equations (8), (11), and (13), respectively, in *Allen et al*. [1998]. Hourly values of $R_n - G$ were estimated from available measurements of global (incoming shortwave) radiation and from computed extraterrestrial radiation following the recommendations for hourly periods on pp. 54–55 (soil heat flux) and 74–75 (radiation) in *Allen et al*. [1998].

The required input data were obtained from the closest grassland weather station (TERENO station Schöneseiffen) 3.5 km to the east of the Wüstebach catchment at 610 m a.s.l.. Global (incoming shortwave) radiation was measured by a CMP3 sensor (Kipp and Zonen, Delft, Netherlands). Air temperature, vapor pressure, atmospheric pressure, and wind speed were all measured at 2 m a.g.l. by a combined transmitter including capacitors and a two-dimensional sonic anemometer (WXT510, Vaisala, Helsinki, Finland). The 1049 h (4%) of data were missing; these were filled by linear regression predictors from the same variables measured by an identical station 40 km to the north (TERENO station Selhausen). Seven remaining hours (0.03%) of data missing simultaneously at both stations were gap-filled by the monthly mean diurnal cycle method; that is, by the average of all available measurements for the respective month of the year and hour of the day.

Except for their use in the gap-filling of actual evapotranspiration (see below), these hourly *PET* estimates were only used as daily sums (mm).

2.4. Actual Evapotranspiration *ET*

Actual Evapotranspiration *ET* was measured near the top of a 38 m tower in the Wüstebach catchment [*Drüe et al*., 2012] by the eddy-covariance technique:

$$ET = \rho \frac{\sum_{i=1}^{N} [(w_i - \bar{w})(q_i - \bar{q})]}{N-1} \quad (2)$$

Here, w is the vertical wind component (m s^{-1}) and q specific humidity (kg vapor per kg air), both measured N (here, 36,000) times during each flux calculation interval (30 min); an overbar denotes averaging over this interval. The micrometeorological tower measurements started shortly after the start of the study period; measurements of parameters associated with radiation, the vertical temperature and wind profile, and the soil were added stepwise in the following (section 3). The wind vector was measured by a CSAT3 ultrasonic anemometer (Campbell Scientific, Logan, UT, USA) facing toward 182° on a 1.5 m long beam at 38 m a.g.l., about 10 m above the tree canopy. Humidity and CO_2 fluctuations were measured by a Li-7500 open-path infrared gas analyzer (Li-Cor, Lincoln, NE, USA) 0.15 m away from the center of the anemometer. Data were logged at 20 s^{-1} and processed with the software ECpack [*van Dijk et al*., 2004] and a custom additional pre/postprocessor matching the scheme suggested by *Mauder et al*. [2013]. In order to filter for high-quality data and align the half-hourly primary output of our flux processing scheme with the hourly *PET* data, we calculated hourly averages of all (i.e., 1 or 2) available latent heat fluxes that received the best flag (flag 0) of the above scheme. Intermediate (flag 1) data were only considered if two such values, both above −100 W m^{-2}, were available in the respective hour. Data with a northern wind direction representing anemometer backwind through the tower structure (343°–25°) were already excluded during the processing. Due to the prevailing southwesterly winds this applied to only roughly 8% of the time. The combined portion of data that were either missing or dismissed was 54%, and thus quite high. They resulted mainly from poorly developed nighttime turbulence, the limitations of the open-path analyzer during wet conditions, and power failures especially during the first winter period.

Hours without logged data or not fulfilling these criteria had to be gap-filled to obtain the continuous data set required for our analysis. Our gap-filling used the already available potential evapotranspiration *PET* as predictor, by fitting a zero-intercept linear regression of high-quality *ET* versus *PET* values, the slope of which gives a robust estimate of the ratio *ET*/*PET*. This ratio, while also containing any hypothetical systematic error in the determination of either *ET* or *PET*, basically equals the product of the unknown "crop" coefficient k_c for spruce forest, and the unknown water stress coefficient k_s [*Allen et al*., 1998]. Especially due to the latter factor, the ratio can be expected to vary with soil water content and plant development on the long term (daily to monthly) and, to a lesser extent, also with stomatal response on a subdaily scale. Ignoring the latter for practical reasons, a step-function time series of $k = k_c \times k_s$ can be found by computing the root mean square error (*RMSE*) of the abovementioned regression for all possible window lengths beginning at the start of the study period between a given minimum and maximum (in our case, 24 h and 180 days, respectively), and picking the window yielding the lowest *RMSE* as the first subperiod of assumedly constant k. This procedure was repeated with the remainder of the study period until all hours were assigned to a subperiod and a k value. The last remaining fragment shorter than the given minimum was included to the last subperiod. Now, missing *ET* values could be estimated by multiplying the k value of the subperiod comprising the gap with the instantaneous *PET* value. Since the regression fitting and gap-filling was executed on the hourly time scale, the approach may be expected to avoid biases in the final daily sums caused by uneven distribution of missing hours in the diurnal cycle, similar as a mean diurnal variation (MDV) approach [see e.g., *Moffat et al*., 2007], but with the exception of the neglected diurnal variation of stomatal response. At the same time, unlike a MDV approach, it avoids concatenating multiple identical cycles during longer data gaps, since the *PET* input reflects the impact of changing weather conditions on evapotranspiration. As a less desirable side effect of this strategy, high-biased artificial correlations between *ET* and *PET* may be introduced.

2.5. Soil Water Content θ

Soil water content within the Wüstebach catchment was measured by the wireless distributed sensor network SoilNet. From the total number of 150 sensor nodes, we selected 109 locations due to their continuous

operation within our study period (Figure 1). Each sensor node measured temperature and volumetric water content θ in three depths (5, 20, and 50 cm) by six ECH_2O probes (EC-5 and 5TE, Decagon Devices, Pullman, WA, USA). In each depth, two sensors were paired with a distance of typically 5 cm to increase the measurement volume and to enable crosschecking. For this study, the arithmetic mean was used to derive average soil water content for each depth at each location. Details on the calibration and signal processing of the probes are given in *Bogena et al*. [2007, 2010] and *Rosenbaum et al*. [2012]. SoilNet measured soil moisture several times each hour with changing intervals (on average 4 times per hour). In order to obtain a time-consistent data set, these values were hourly averaged using the arithmetic mean. In case of data gaps (typically $\leq$2 days), e.g., due to frozen soil conditions or transmission failures, we used linear interpolation for gap-filling. This gap-filled hourly data set was than averaged to daily values for this study using the arithmetic mean. Where we report horizontal area averages or standard deviations for a single depth level, it was assumed that the respective arithmetic operation on the 109 values provides a reasonable estimate of the true area statistics without weighing. Where we report column averages using all three depth levels, in contrast, weights were introduced to account for the uneven distribution of depths. We assumed that the 5 cm sensor represents the layer from the surface to a depth of 10 cm, the 20 cm sensor the layer 10–30 cm, and the 50 cm sensor the layer 30 cm–1 m, and weighted accordingly. Where we report the day-to-day rate of change of θ, the value for each date is based on the difference between the following and the proceeding day, divided by 2. This procedure ensured that change rates are centered on (rather than between) days, consistently with all other variables. As a side effect, it provided a low-pass filter: Since change rate calculation is based on differences occurring over 48 rather than 24 h, fluctuations shorter than 2 days were suppressed.

2.6. Runoff *R*

Runoff discharge was monitored at two sites (one at the outlet and one within the catchment). For the accurate measurement of river discharge, a combination of Parshall flumes and V-notch weirs is used. In both devices, water flow is measured by the water level using pressure transducers and logged in a 10 min interval. While the Parshall flume is used to measure normal to high flows (5–300 L/s), the V-notch weir is specifically dedicated to measure low-flow conditions (<5 L/s). The catchment area for translation of discharge into precipitation equivalent, based on a 1 m resolution digital elevation model, is 38.520 ha. Here, we focus on runoff at the catchment outlet.

2.7. Empirical Orthogonal Functions (EOFs) of Soil Water Content Patterns

In order to represent changes in the spatial pattern of θ by less than the original data set (109*3 variables), we applied principal component analysis to the matrix of 327 measurement locations and 1096 days. Principle component analysis expresses a data matrix Y, each column of which must average to zero due, e.g., to a prior removal of the means, as a linear combination of new, statistically independent (orthogonal) columns Y' and their loadings (eigenvectors) E; in matrix notation:

$$Y = Y' \times E^T, \tag{3}$$

where the superscript T indicates the matrix transpose. The first column of Y' describes as much as possible of the variance of Y, and can be used together with the first row of E^T as a memory-saving representation of a noise-reduced version of Y; the second and any further column of Y' describe as much as possible of the remaining variance. If the matrix Y consists of a single variable, but different realizations in time (e.g., rows) and space (e.g., columns), the principal components are also known as empirical orthogonal functions (EOFs), and the loadings sometimes as expansion coefficients [e.g., *Perry and Niemann*, 2008]. Based on the analysis of spatial versus temporal variance that will be presented in section 4.3, we chose the orientation of our EOF analysis such that only the small portion of variance associated with temporal changes of the area average had to be removed. Consequently, the transformed data set consists of statistically independent (orthogonal) maps and nonorthogonal time series of the coefficients required to regain the measured soil water content pattern as a linear combination of those maps. Examples of the application of EOF analysis to similar data sets including a more detailed description of the underlying theory are given in *Perry and Niemann* [2008], *Korres et al*. [2010], and *Graf et al* [2012]. Based on the amount of variance they explain according to section 4.3, we only used the first two EOFs and

loading time series. By cluster analysis of the loadings (squared Euclidean k-means clustering), we assigned each day to one of two clusters such that loading variance within each cluster was minimal. Consequently, the centroid of each cluster consisted of two loading values (one each for EOF 1 and 2) representing the average weight of the two EOFs for all days within one cluster. For each of both clusters, the most typical spatial pattern of θ in original units could now be reconstructed by multiplying the centroid loadings with the two EOFs and adding the average of the spatial averages of all days assigned to the respective cluster. The procedure was implemented in GNU Octave, using the functions "princomp" and "kmeans" for the EOF and cluster analysis, respectively.

2.8. Wavelet Coherence Analysis

Ordinary correlation and regression analysis provide global parameters for the quantification of relations between two variables, some of which will be presented in the following results sections as a consequence of the application of the methods described above. Cross-correlation analysis can extend such insights to also account for lagged responses that might be expected between, e.g., rainfall, soil water content at different depths, and runoff. However, the time lag in this case is another global parameter of the data set, which cannot vary with time or time scale. A spectral transformation such as the Fourier transform provides a separate quantification of all these parameters for different time scales, but assumes they are stationary in time. As a method to quantify both the strength and lag of a correlation in nonstationary data sets simultaneously for each point in the time and frequency domain, wavelet analysis has increasingly been used in various fields of geosciences. Applications of wavelet analysis include field-scale time series [e.g., *Vargas et al*., 2010], catchment studies [*Lauzon et al*., 2004], model validation [*Schaefli and Zehe*, 2009], and combinations with EOF analysis [*Parent et al*., 2006]. The (continuous) wavelet transform of a time-dependent variable *y(t)* for a specific location along the time axis τ and a specific time scale *s* is given by:

$$W(s,\tau)=\int_{-\infty}^{\infty} y(t)\cdot\frac{1}{\sqrt{s}}\psi*\left(\frac{t-\tau}{s}\right)dt \tag{4}$$

[*Si*, 2008]. Here, $\psi*$ is the complex conjugate of the mother wavelet ψ, which can be chosen from a variety of functions. The choice of the mother wavelet can have a considerable impact on the results of a wavelet analysis [*Torrence and Compo*, 1998]. In absence of more specific reasons, the continuous, nonorthogonal Morlet wavelet is a reasonable choice for many geosciences applications since it offers comparable resolutions in the time and frequency domain, and its time scale *s* is almost exactly equal to its equivalent Fourier period [*Grinsted et al*., 2004]. In practice, the integration over an infinite time domain indicated in equation (4) can only be performed from the start to the end of the available time series. This causes edge effects in the wavelet transforms for certain combinations of *s* and τ—for the largest time scales, a reliable wavelet transform only exists near the center of the time series. This region, also termed the "cone of influence," will be highlighted in the results section.

The wavelet transforms of two simultaneously sampled variables can be used to compute the cross wavelet spectrum, an analog of the covariance in ordinary correlation/regression analysis and of the cross spectrum in Fourier analysis [e.g., *Mauder et al*., 2007]. In wavelet coherence analysis, the real part of the cross wavelet spectrum is normalized to provide an analog of the R^2 value. In contrast to the conventional R^2, it is localized in the time and frequency domain and assumes that any lag between both variable has been removed. Like a conventional R^2, however, it is restricted to the linear part of that relation. The imaginary part is used to give a phase angle quantifying this lag, which may vary again both in the time and frequency domain. Descriptions of the Morlet wavelet, as well as the equations for efficient wavelet transform computation, the cross wavelet spectrum, wavelet coherence, and the required smoothing, are given, e.g., in *Torrence and Compo* [1998], *Grinsted et al*. [2004], and *Si* [2008]. The Matlab™ software package we used for these steps is described in *Grinsted et al*. [2004], including the Monte Carlo approach used to determine the significance of localized coherence. It should be noted that recently, the Hilbert-Huang-Transform [e.g., *Koch et al*., 2010] and its extension to multivariate data sets [*Hu and Si*, 2013] have been tested on runoff and soil water content data sets as an even more assumption-free, data-adaptive alternative. In this study, however, we confine ourselves to wavelet analysis as the simplest, and more established, technique that can be used to yield robust results on the questions at hand.

Table 1. Statistics of a Comparison of Our *P* and *PET* Data Sources (Sections 2.2 and 2.3) to Measurements Within the Catchment (Section 3), Which Were Only Available Near (*PET*) or After (*P*) the End of the Study Period[a]

Parameter	*P*	*PET*
Period	4 Jan. 2014 to 8 Feb. 2014	18 Jun. 2012 to 30 Apr. 2013
Bias (mm days^{-1})	0.1	0.1
Bias (% of average)	2.1	5.3
MAE (mm days^{-1})	0.7	0.2
RMSE (mm days^{-1})	1.0	0.2
R^2	0.95	0.98
Regression offset (mm)	−0.2	0.15
Regression slope	1.09	0.96
95% C. I. (±)	0.09	0.02

[a]Within-catchment measurements are the reference (x) variable, such that a negative bias and a slope < 1 indicate underestimation and vice versa. MAE: Mean absolute error; RMSE: Root mean square error; 95% C. I.: 95% confidence interval of slope (±).

3. Ability of Point Measurements to Represent Catchment Conditions

As mentioned in sections 2.2 and 2.3, due to the difficulty of finding gapless input data for our test site we used continuous precipitation data from an official weather service station and *PET* input data from a nearby grassland station at a distance of 8 and 3.5 km, respectively. Also, the eddy-covariance measurement of *ET* (section 2.4) was performed at a single point within but near the edge of the catchment, with a footprint (area of influence) that varied in time due to changes in wind direction and other meteorological conditions. In this section, we use additional sources of information to frame the uncertainty resulting from these limitations.

For reference measurements of precipitation, a pluviometer (Pluvio^2, Ott, Kempten, Germany) was recently installed inside a deforested area (data available since 4 January 2014). To test the representation of the *P* data used for this study, we compared the DWD data with the Pluvio^2 for a period of about 1 month. We applied the same diurnal aggregation and the same DWD correction (section 2.2), but with the appropriate horizon elevation angle class for the deforested site (5°). The statistics of the comparison indicate a good agreement of both data sets (first column in Table 1). However, the confidence intervals of the regression slope indicate considerable uncertainty. In the lower 95% confidence limit, the station Kalterherberg would exhibit an approximate 1:1 relation, while in the upper limit it would overestimate in situ *P* by 20%. Given the shortness of the comparison period we did not attempt to correct *P*. The uncertainty should be kept in mind when assessing the catchment water budget closure in the following section 4.1.

Potential evapotranspiration *PET* estimation requires radiation measurements, which were not available on-site for most of the study period. However, starting from 18 June 2012, i.e., for approximately the last 10.5 months of the study period, radiation was measured (NR01, Hukseflux, Netherlands) at the top of the eddy-covariance tower and thus within the catchment (Figure 1). To test the transferability of *PET* from the 3.5 km far grassland station to the Wüstebach site, we repeated the FAO procedure referred to in section 2.3 [*Allen et al*., 1998] on the available tower values of global (incoming shortwave) radiation, temperature, humidity, wind speed, and pressure. Table 1 shows that the resulting daily sums at the tower location compared well to those of the grassland station. This indicates that reference *PET* computed from data of the grassland station 3.5 km away represents grassland reference *PET* in the catchment reasonably well. We assume that the better agreement compared to *P* is mainly due to the longer time period, the shorter distance and the lower spatiotemporal variability of the *PET* input data. However, it should be kept in mind that this apparent high confidence in *PET* is overridden by the uncertainty of using grass reference *PET* as a surrogate for the unknown forest *PET*.

The area of influence of eddy-covariance measurements, and thus of our *ET* data, can be estimated using a flux footprint model [*Hsieh et al*., 2000; *Kormann and Meixner*, 2001]. We applied the model configuration described in detail in *van de Boer et al*. [2013] to a rectangle of 2 km by 2 km centered on the eddy-covariance tower with a resolution of 2 m. Based on the catchment geometry and aerial views, each grid point was classified as either a part of the catchment (target 1), similar spruce-dominated forest outside the catchment (target 2), or nontarget land-use type (target 0). Due to the remote situation of the catchment, the latter consisted mostly of past clear-cuts, aisles and roads, and some grassland especially to the south-east; no settlements, lakes, or croplands were found in the rectangle. The footprint model was run for every hour with nongap-filled *ET* data of the study period. Figure 1 gives an overview of the footprint cumulated in both space and time [cf. *Chen et al*., 2009]. Between single hours, the contribution of the catchment area to the tower measurement ranged between zero and 100%, while the joint contribution of target 1 and 2

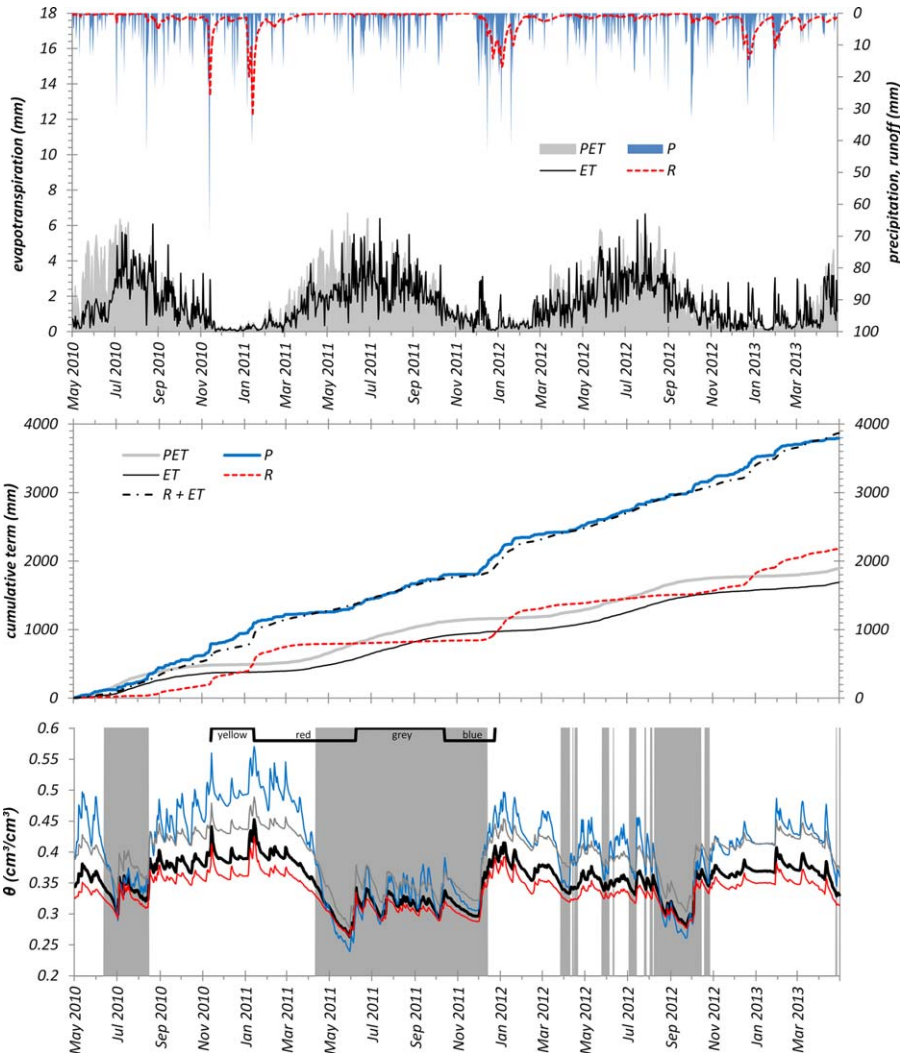

Figure 2. (top) Daily and (middle) cumulative time series of the catchment water budget components precipitation (P), runoff (R), and Evapotranspiration (ET), along with potential grass reference evapotranspiration (PET); (bottom) daily averaged soil water content at the three depth levels (blue/top: 5 cm, gray/middle: 20 cm, red/bottom: 50 cm) along with their weighted depth average (bold black, see section 2.5). The background shades (pattern cluster: white 1, gray 2) and the bar with color names are for later reference in section 4.3.

was always above 55%. Averaged over the study period, the contribution of the catchment area to the tower measurement was 62%, and the joint contribution of target 1 and 2 was 96%.

4. Results and Discussion

Figure 2 gives an overview of the time series of the most important variables discussed in this study, which will be repeatedly referred to in the following subsections. It depicts the typical annual cycles with predominantly slightly increased winter precipitation.

4.1. Annual Water Budget

The water balance of an arbitrary section of land surface is given by

$$P = R + ET + \Delta S, \tag{5}$$

where ΔS is the storage term. Since the conductivity of the aquifer bedrock is on the order of 10^{-9} to 10^{-7} m s^{-1} according to the hydrogeological map of North Rhine-Westphalia [*HK100*, 2009], we neglect deep

Table 2. Water Budget Components of the Wüstebach Catchment for the Total Period and Annual Subperiods[a]

	Period	*P* (mm)	*PET* (mm)	*ET* (mm)	*R* (mm)	residual (mm)	residual/*P*	*R*/(*P* – *res.*)
1	May 10 to April 11	1259	656	484	791	−16.5	−1.3%	62.0%
2	2011	1172	672	596	621	−44.1	−3.8%	51.0%
3	May 11 to April 12	1260	634	609	596	54.9	4.4%	49.5%
4	2012	1386	615	606	807	−27.7	−2.0%	57.1%
5	May 12 to April 13	1274	600	595	793	−114.0	−8.9%	57.1%
6	Total Period, p.a.	1264	630	563	727	−25.2	−2.0%	56.3%

[a]The first four columns are rounded off for convenience while the residual (*P-ET-R*) and its relative value are based on raw data.

percolation, thus *R* can be approximated by the river discharge measured at the gauge at the catchment outlet (section 2.6), divided by the catchment area. At the spatial scale of our catchment, *P* is typically approximated by a single point measurement, which is in our case additionally supported by the relatively good agreement between two gauges in a short-term comparison (section 3). Due to the homogeneous, even-aged forest vegetation, we assume that the same applies to *ET*, which is a weighted average over a varying footprint rather than a point measurement in the strict sense (section 3). Finally, at the temporal scale of a year or more, it is common to neglect the storage term, which will be discussed in more detail in section 4.2. Unlike in most gauged catchments, where *ET* is determined residually, we therefore have at hand measured local or nearby estimates of all major contributions to test the water balance closure. Table 2 gives annual sums and Figure 2 the corresponding time series.

On average, the precipitation was partitioned into about 44% evapotranspiration and 56% runoff. The residual of the balance was within ±60 mm or ±5% of precipitation for all annual subperiods shown in Table 2, except for the period May 2012 to April 2013. During this period, considerably more water was removed by evapotranspiration and runoff than provided by precipitation, which may be a result of either measurement uncertainty or storage term depletion. For the total 3 year period, the residual was 2%. This indicates that remaining changes in the storage term, which could still be significant in single exceptional years, leveled out on an interannual scale. In most shown subperiods as well as on average, the residual was negative, i.e., there was slightly less precipitation than required to account for evapotranspiration and runoff. However, all residuals including the most extreme ones are within the range of uncertainty expected for precipitation measurements (section 3), and especially for *ET* determination due to the combined effect of multiple shortcomings such as the energy balance closure problem [*Foken et al*., 2011], data gaps (section 2.4), and spatial representation [e.g., *Chen et al*., 2009]. An early effort to close a catchment water budget using micrometeorological *ET* measurements was published by *Högström and Larsson* [1968] for an agricultural catchment in southern Sweden. At the time, the eddy-covariance technique was just emerging, and the authors used sample measurements outside the catchment during selected hours to calibrate a profile method, and ultimately an estimation of *ET* from *PET* by seasonal *k* factors. They noted that the water budget residual of approximately −8% they arrived at, was balanced by the expected underestimation of precipitation. This is in good agreement with our finding of an approximately closed water balance with precipitation data including the *Richter* [1995] correction (section 2.2), which amounted to +7% in our case. *Wilson et al*. [2001] compared eddy-covariance measurements of *ET* to estimates from *P-R* for a forested catchment in the southeastern United States. They found a good agreement between both estimates, which was, however, overridden by the uncertainty resulting from incomplete energy balance closure of 80% of the eddy-covariance measurement. The cause of the energy balance closure gap between the turbulent fluxes (sensible heat flux H + latent heat flux λET) and available energy is subject to debate [*Foken et al*., 2011]. For our study period, the energy balance closure is unknown, but the radiation measurements installed near the end of the study period (section 3) indicate an energy balance ratio higher than 80%, depending on the unaccounted storage term. Evapotranspiration was 89% of potential grass reference evapotranspiration on average. Occasionally *ET* reached or exceeded *PET*. However, the specific potential evapotranspiration of spruce forest, due to its albedo, may be higher than *PET*, which we chose as a reference here for its rigid definition, well-defined aerodynamic resistance, and comparability to other studies. Even so, the catchment and period can clearly be characterized as a dominantly energy-limited ecosystem, where *ET* is typically limited by the available energy input by radiation rather than by water availability. In the Budyko framework [*Budyko*, 1974], all annual periods were close to expectations from theory and global data syntheses (Figure 3), and close to the demand limit due to their low ratio *PET/P*.

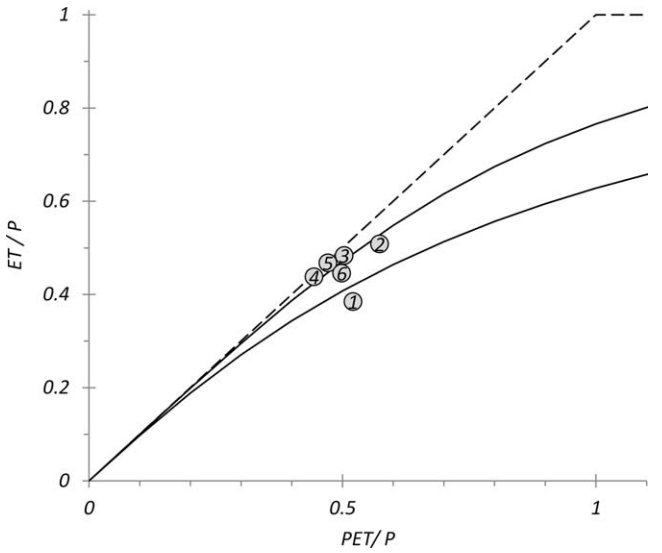

Figure 3. Budyko plot of the annual ratios of actual and potential evapotranspiration over precipitation. Numbers in the circles refer to the row number in Table 2; the dashed line depicts the theoretical limits and the two solid lines an uncertainty range from different global synthesis studies recently summarized by *Williams et al.* [2012].

Among the few and typically short periods of a less strict energy limitation and more severe water limitation observable as a divergence between *ET* and *PET* in Figure 2, the longest periods were found in the spring seasons of 2010 and 2011. For a better localization of such events in the time and frequency domain, Figure 4 shows a wavelet coherence plot (see section 2.8) of actual versus potential evapotranspiration.

The coherence between *ET* and *PET* was primarily subject to the common annual cycle of both variables (periods $>$ 200 days), and to intermittent close relations on much shorter time scales ($<$1 month). Delays and anticorrelations between both variables were absent or small, and inconsistent where they occurred, with the exception of the region affected by edge effects of the wavelet methodology. The spring period 2010 was affected by gap-filling of *ET*, but the spring and summer period 2011 showed indeed a lower-than-average coherence between *ET* and *PET*. This suggests that *ET* increasingly depended on resources not represented by *PET* such as soil water content, as may be expected in a more water-limited situation. The coherence breakdown is observed best in Figure 5, which shows the time series of period-averaged coherence from Figure 4. During spring and summer 2011, *ET* increasingly decoupled from *PET*, leading to a coherence minimum during autumn 2011. At the same time, coherence between the ratio of both (i.e., the relative evolution of the inferred water stress coefficient k_s, see section 2.4) and soil water content increased.

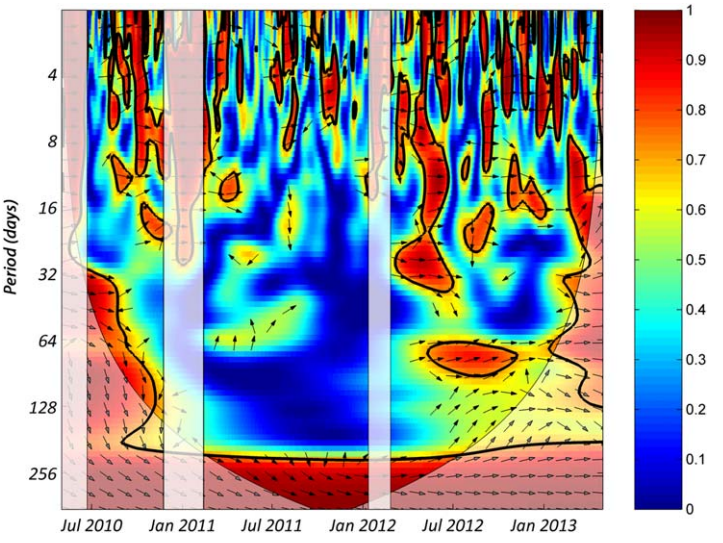

Figure 4. Wavelet coherence plot between ET and PET. The local R^2 (in the frequency and time domain) between both variables is color-coded as indicated by the bar to the right; significant correlations on a 95% confidence level are surrounded by a bold line. Lighter coloring bordered by a thin line indicates the conical regions subject to edge effects and periods with high-biased R^2 due to longer filled data gaps in ET. Arrows indicate the phase angle of the relation (where $R^2 > 0.5$); an arrow to the right indicates delayless correlation, an arrow to the left anticorrelation, a downward arrow a delay in ET, and an upward arrow a delay in PET.

4.2. Role of Storage Term in Water Balance Closure on Shorter Time scales

The storage term ΔS in equation (5) results from water content changes in various ecosystem compartments:

$$S = S_{aqu} + S_{vad} + S_{sur} + S_{veg} + S_{int} \quad (6)$$

where the different indices indicate the following compartments: *aqu* = aquifer, *vad* = vadose zone including the litter layer, *sur* = surface (water body or snowpack), *veg* = within vegetation, *int* = canopy intercepted water.

S_{int} is constrained by the interception capacity; for this

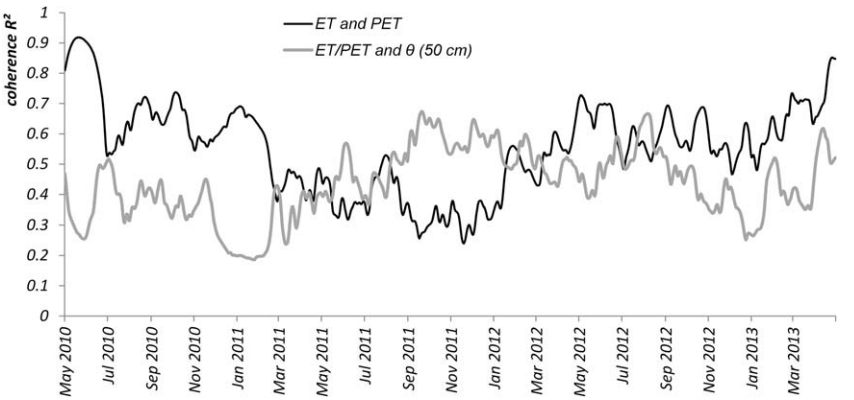

Figure 5. Time series of period-averaged coherence between actual (PET) and potential (ET) evapotranspiration, and between their ratio and horizontally averaged soil water content at the 50 cm depth level.

parameter *Rutter and Morton* [1977] reported a maximum of 2 mm based on various field studies in midlatitude and high-latitude forests including spruce. Due to the absence of water bodies other than the river system, S_{sur} can be constrained to fall below the same maximum during summer, but in winter snowpacks may cause a considerably higher storage. Local sample measurements of snowpack height, tree diameters, and sap flow have been started in the meantime, but are not consistently available for the study period. The same applies to eight groundwater well measurements of S_{aqu}, of which only one sufficiently covered the study period. However, we found only low correlations of the water level time series with catchment-wide soil moisture measurements. We attribute this discrepancy to the fact that the water table at this site frequently reached the surface, which did not happen in most of the catchment area. For this reason we did not include the groundwater well measurements into the analysis. S_{vad}, however, is represented by the three depth levels of the soil water content monitoring network (section 2.5). The measurement signal of each is related linearly by an unknown but constrained coefficient to a part of the storage term:

$$S_{vad}(t) = \int \theta(x,y,z,t)dxdydz \approx \sum_{i=1}^{N} c_i\theta(i,t) + \varepsilon \tag{7}$$

Here, t is time, z depth, the integral refers to the three-dimensional domain defined by the catchment boundaries, the soil/litter surface, and the bottom of the active aquifer, and θ is volumetric water content. In the discrete version on the right-hand side, i is the number of a sensor, c_i an empirical coefficient representing the three-dimensional domain which is well represented by this sensor, and the residual ε is the part of S_{vad} not represented well by any of the sensors. In a one-dimensional framework where each sensor level is represented by one horizontally averaged water content, x and y are obsolete, the dimensions of S and c_i change from m^3 to m, and i becomes the number of the sensor level (e.g., 5, 20, and 50 cm in our case). Since the change rate of S, ΔS, equals the residual of the major water budget components, *P-R-ET* (equation (5)), the time derivative of soil water content should be linearly related to this residual. However, random errors in each of the terms *P, R, ET*, and θ as well as the unaccounted storage terms S_{aq}, S_{sur}, S_{veg}, and S_{int} will affect the scatter in this relation. Figure 6 demonstrates this relation based on daily values. The scatter was considerable and the "best" horizontally averaged soil water content (50 cm) explained only 40% of the variance. At 20 cm, R^2 amounts to 0.39, and at 5 cm to 0.37 (not shown).

Random errors as well as storage terms with a small, finite maximum such as S_{int} tend to cancel out on longer time scales, and snowpacks did not occur in the study site during summer. These or other, unexpected error sources acting on a particular time scale or at particular times might contribute to the scattered relation observed on daily data from the whole study period. Instead of testing a large number of temporal aggregation schemes or time windows, wavelet coherence analysis (section 2.8) can be used to inspect whether the moderate global correlation evident in Figure 6 was caused by a breakdown of coherence on small time scales, in winter, or at any other, unexpected time scale or time.

Figure 7 demonstrates that coherence on intermediate time scales (4–30 days) regularly broke down in winter, though not exclusively so. Independent of season, significant correlations rarely extended to periods

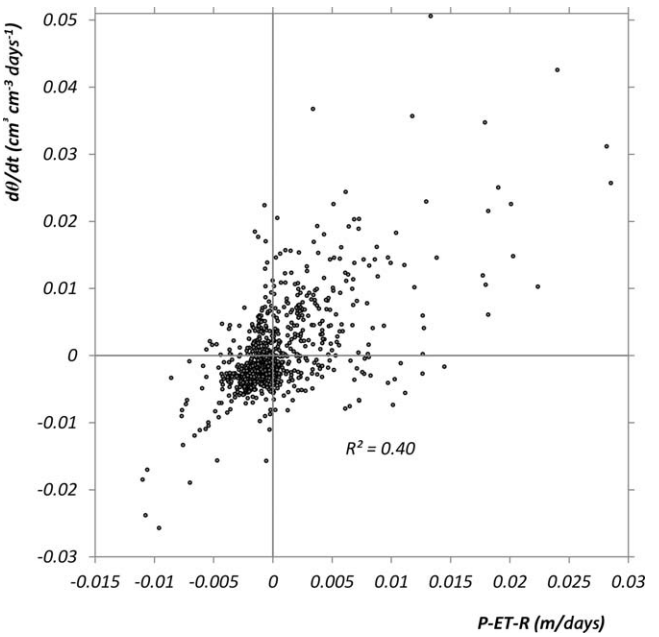

Figure 6. Time derivative of volumetric soil water content at 50 cm depth versus the water balance residual.

shorter than 4 days, and between 4 and 8 days considerable but unsystematic phase delays were still present. This suggests that the ordinary correlation/regression analysis attempted in Figure 6 will be more successful on an aggregated data set based on week sums, representing variability at the weekly time scale and longer only. Fluctuations on shorter time scales, which were hypothetically caused by measurement uncertainty and unaccounted "fast-turnover" storage reservoirs, are suppressed in such a data set. Figure 8 gives the analogy to Figure 6 based on such an aggregated data set.

Explained variance at weekly resolution increased for all soil water content variables: At 20 cm, R^2 is 0.58, and at 5 cm 0.52. The fact that correlation is again highest for the 50 cm depth level is in rough agreement with findings by *Lauzon et al.* [2004], who found in another catchment a correlation maximum at a depth of 35 cm. In a multiple regression regarding all storage components (including unknowns not cancelled out by the low-pass filtering, such as the effect of snowpacks or catchment-wide groundwater levels), the slope coefficient of each storage term proxy should provide an estimate of its c_i value, or its minimum in case of considerable residual scatter (see *Webster* [1997] and Figure 8). The coefficients of the three soil water content depth levels, as proxies of S_{vad}, would then be an estimate of the thickness of the domain for which the sensor level is representative. In our case, a stepwise backward multiple regression with all three SWC levels, eliminating in each step the most insignificant parameter with a confidence level $<$95%, yielded the final result:

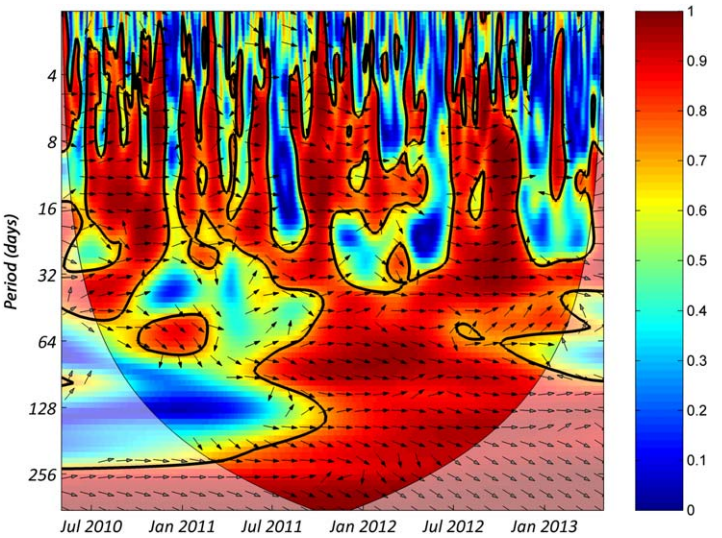

Figure 7. Wavelet coherence plot between P-R-ET and the time derivative of volumetric soil water content at 50 cm. Same presentation as in Figure 4.

$$P-R-ET_a=\Delta S = 0.13\frac{d\theta_{5cm}}{dt}+0.86\frac{d\theta_{50cm}}{dt} \quad (8)$$

with $R^2 = 0.63$. Not only the regression offset, but also the 20 cm depth level was eliminated, apparently because it is well represented by its upper and lower neighbor. The empirical coefficients indicate that SWC in the upper 13 cm of the soil is represented best by the 5 cm sensor level, while the 50 cm sensor level represents a layer from 12 cm to about 1 m depth. This is in fair agreement with the a priori rule presented in section 2.5 for estimating the

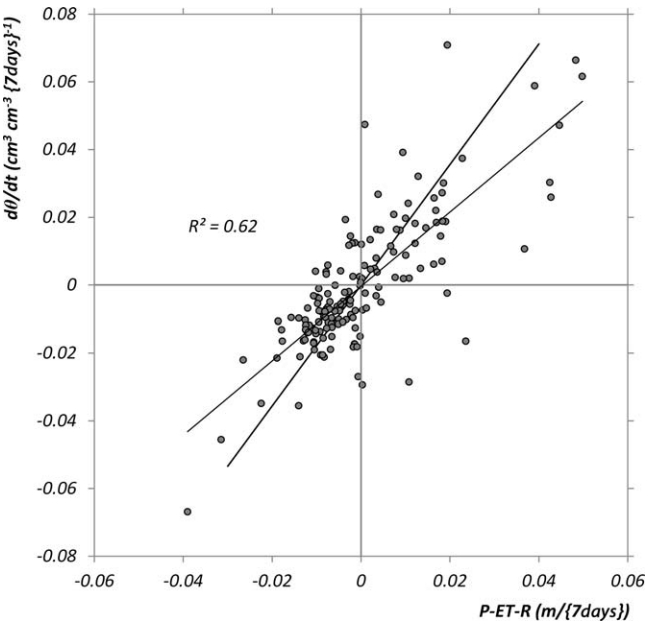

Figure 8. As Figure 6, but for weekly sums of both variables. Also shown are the two regression lines obtained by choosing either axis as dependent variable, which frame the slope of the underlying functional relation between both variables [*Webster*, 1997].

SWC of the upper meter of the soil as a weighted average, which is used, e.g., in Figure 2. The fact that the 50 cm sensor level contributed most to the inferred storage change in a 1 m deep soil layer is also in agreement with recent findings by *Hu and Si* [2014] of column-averaged soil water contents being approximated best by sensors in the middle of the profile. Ideally, further SWC sensors below the 50 cm level and a dense net of groundwater wells would be required for a complete characterization of the storage term, including saturation pools at the soil-bedrock interface [*Tromp-van Meerveld and McDonnell*, 2006].

4.3. Spatiotemporal Patterns of Soil Water Content and Their Relation to the Hydrological State of the Catchment

In section 4.2, it was demonstrated that soil water content θ can help to close the catchment water budget on subannual time scales. Although this task requires the spatial average of θ only, any reduction of the considerable measurement effort associated with the sensor network, either by a sparse sensor arrangement or by spatially distributed modeling, would require insight into the spatial pattern. From a process-oriented point of view, it is also relevant whether a change in the spatial average is caused by similar, simultaneous changes at all points, or whether it is the net effect of a true change in the actual pattern.

The soil water content measurements at 327 points in space (109 end device sites with 3 depths each) and 1096 days in time can be represented by the following decomposition [e.g., *Graf et al.*, 2011]:

$$\theta(t,i)=\bar{\tilde{\theta}}+\tilde{\theta}'(t)+'\bar{\theta}(i)+\varepsilon(t,i) \tag{9}$$

where t is time and i the measurement point in space. Straight overbars denote temporal averaging, tilde overbars denote spatial averaging, right primes indicate deviations in time and left primes indicate deviations in space; the last term (ε) represents residual fluctuations after removal of all prior terms. Consequently, the terms on the right-hand side from left to right represent the global mean, the time series of space-averaged deviations from it, the map of time-averaged deviations from the global mean, and residual fluctuations in both space and time. Each of the last three terms contributes to the total variance:

$$\sigma^2=\sigma_t^2+\sigma_i^2+\sigma_{res}^2 \tag{10}$$

where σ_t^2 is the purely temporal variance, σ_i^2 the purely spatial, and σ_{res}^2 the residual spatiotemporal variance. In the simplest case of a space and time-variant data set, the value at each point results from the superposition of identical temporal variations occurring at all points, and a time-constant offset at each point. The last term in equations (9) and (10) would be zero and the actual pattern would not vary with time. In our data set, σ_t^2 is 13.8%, σ_i^2 73.4%, and σ_{res}^2 12.5% of the total variance. θ dynamics in our catchment can therefore be described to a considerable degree, but not completely, as a noninteracting superposition of a single spatial pattern and its offset by a single time series.

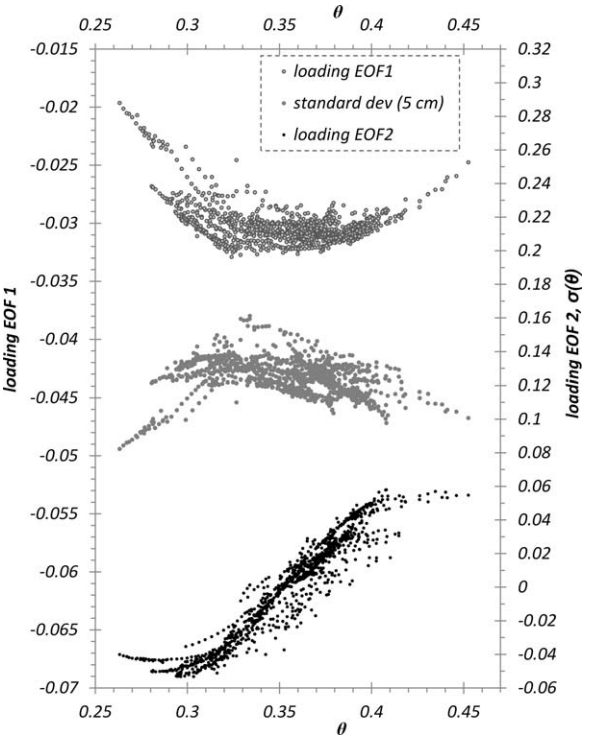

Figure 9. Loadings of the first spatial soil water content EOFs and spatial standard deviation at the 5 cm level versus depth-averaged (see section 2.5) soil water content.

Unlike in other, more specialized variance decompositions [e.g., *Mittelbach and Seneviratne*, 2012], no covariance terms apply in equation (10) because all terms of equation (9) are independent of each other. Any covariance between spatial and temporal anomalies is part of σ^2_{res}. In the second simple-most case of spatiotemporal variability, σ^2_{res} would be nonzero but only result from temporal variations of the spatial standard deviation, while the normalized pattern remains unchanged. In a principal component analysis, this would result in the first component explaining already 100% of variance. Principal component analysis can only be performed on either $\sigma^2_t+\sigma^2_{res}$ or $\sigma^2_i+\sigma^2_{res}$. Due to the dominance of spatial variance in our data set the first alternative, which transforms the different time series into orthogonal new variables (sometimes also referred to as temporal EOF analysis) [cf. *Perry and Niemann*, 2007; *Korres et al.*, 2010] would describe less of the total variance than the second one. Hence we focus on spatial EOF analysis, which describes $\sigma^2_i+\sigma^2_{res}$ as a time-dependent linear combination of time-invariant maps (section 2.7). The maps are orthogonal to each other and describe each as much of the abovementioned variance as possible under this constraint, in descending order. In our data set, EOF1 describes 85.8% of $\sigma^2_i+\sigma^2_{res}$. θ dynamics in our catchment can therefore not be described by temporal variations of the average and standard deviation of a single spatial pattern either. Unlike such a concept, EOF analysis can also describe each instantaneous θ map as a linear combination of two or more underlying patterns. Here we focus on EOF1 and EOF2, which together describe 92% of $\sigma^2_i+\sigma^2_{res}$ and, in combination with σ^2_t, 92.8% of the total variance σ^2. Their loading time series, which are nonorthogonal and can therefore describe overlapping fractions of variance, are related to 16.8% and 90.0%, respectively, of σ^2_t. Two significance tests (Rnd-Lambda and Avg-Rnd) [*Peres-Neto et al.*, 2005] indicated that these two and up to three more EOFs are significant at the 95% confidence level. In similar studies on soil water content [*Perry and Niemann*, 2007; *Korres et al.*, 2010] or soil respiration [*Graf et al.*, 2012], only the first one to two EOFs have been found significant, and EOF1 typically described less of the total variance than in this study. However, in these studies measurements were performed manually and the number of sampling dates was limited to between 13 and 28. The continuously measuring wireless sensor network used here provided the large number of repetitions favorable for significance tests, as well the even temporal separation required for an unbiased quantification of how much of total spatiotemporal variance each an EOF describes. In an EOF analysis of gravimetric soil water content data from two subsites of the SGP97 experiment, *Yoo and Kim* [2004] found up to seven significant EOFs and a portion of variance explained by the first EOF between 60% for the full data set, and up to almost 80% for interstorm periods isolated from the full data set. Against the background of these studies, the θ pattern in our catchment can be characterized as remarkably stable, with 85.8% variance explained by the first EOF in spite of continuous monitoring over 3 years. Hypothetically, the control of quasi-constant spatial properties such as porosity, slope location, and vegetation was higher in our forest catchment than in the above studies, which focused on agricultural and grassland regions with a higher temporal variability of soil water content.

EOF1 mostly describes the time-averaged pattern of soil water content. It always occurred with the same (arbitrarily negative) loading sign. The absence of loading sign changes indicates that this basic pattern

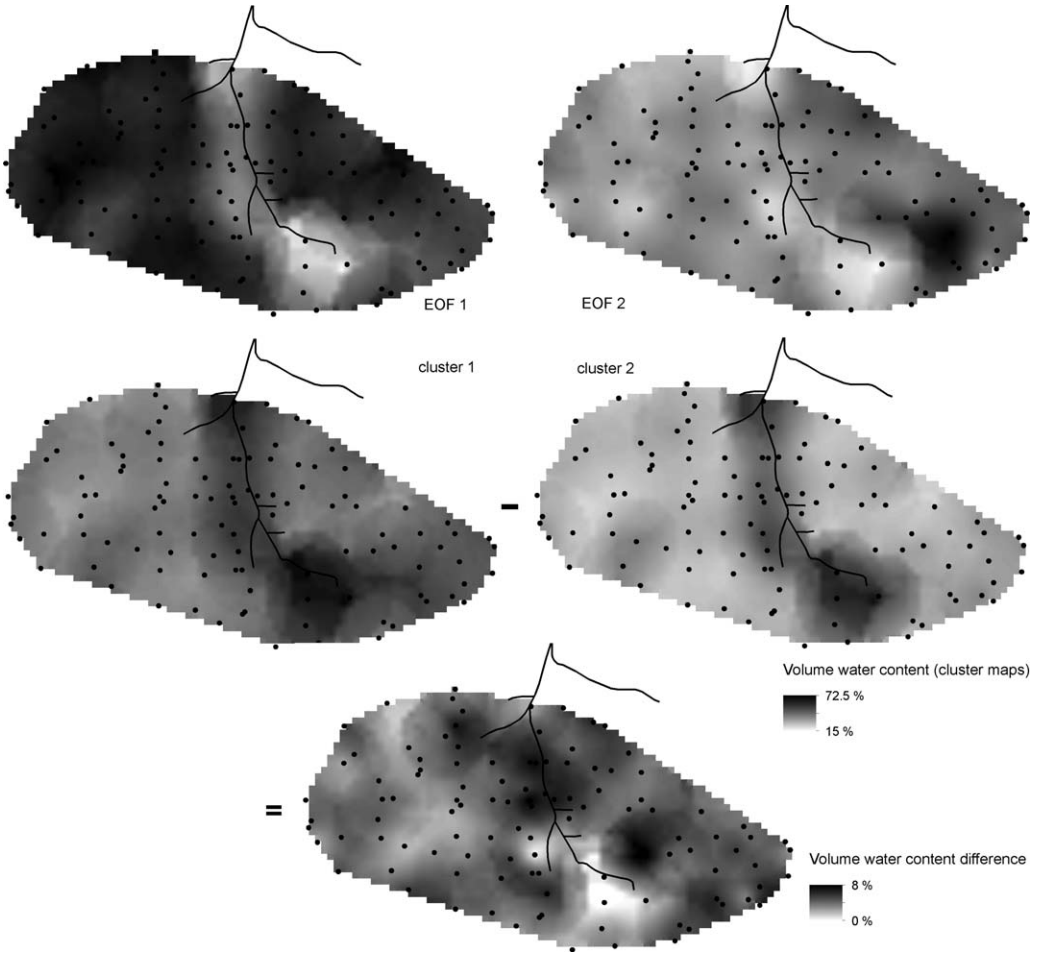

Figure 10. Cluster-based soil water content patterns and difference between them for the 5 cm depth level. EOF and cluster maps are based on discrete values for each SoilNet point but presented as a raster interpolated by ordinary Kriging for convenience; differences are based on this raster.

never was replaced by an inverse pattern, but only occurred with differently strong contrasts, which are described by the magnitude of the loading. Consequently, the dependence of this loading on spatially averaged soil water content shown in Figure 9 qualitatively resembles the relationship of spatial standard deviation and average soil water content [*Vereecken et al.,* 2007; *Rosenbaum et al.,* 2012].

EOF2, in contrast, occurred with positive or negative loadings in time. It was approximately linearly related to soil water content over a wide range, but the pattern variations it describes saturate at extremely high and low water contents (Figure 9).

While EOFs give an impression of spatial patterns underlying a space-time data set, their sign and units are not related to physical quantities without multiplication with each date's loading. One way to extract typical, recurring patterns in the natural units of soil water content is a cluster analysis of these loadings, and subsequent pattern reconstruction with the cluster centroid loadings, as described in section 2.7. The resulting maps are shown in Figure 10. Both patterns are qualitatively similar, as may be expected from the low contribution of σ_{res} and the absent sign changes of the dominant EOF 1 (see discussion and Figure 9 above). Displaying the difference between both patterns as well, however, reveals that cluster 2 was not just an offset version of cluster 1. The smallest differences were found in regions that remained consistently close to saturation in both situations, especially in the source area of the Wüstebach River. Consequently, the soil water content histograms of the two clusters had identical (20 and 50 cm) or close (5 cm) maxima, but differed in terms of their minima, average and median, which are lower in the "dry" cluster (Figure 11). This

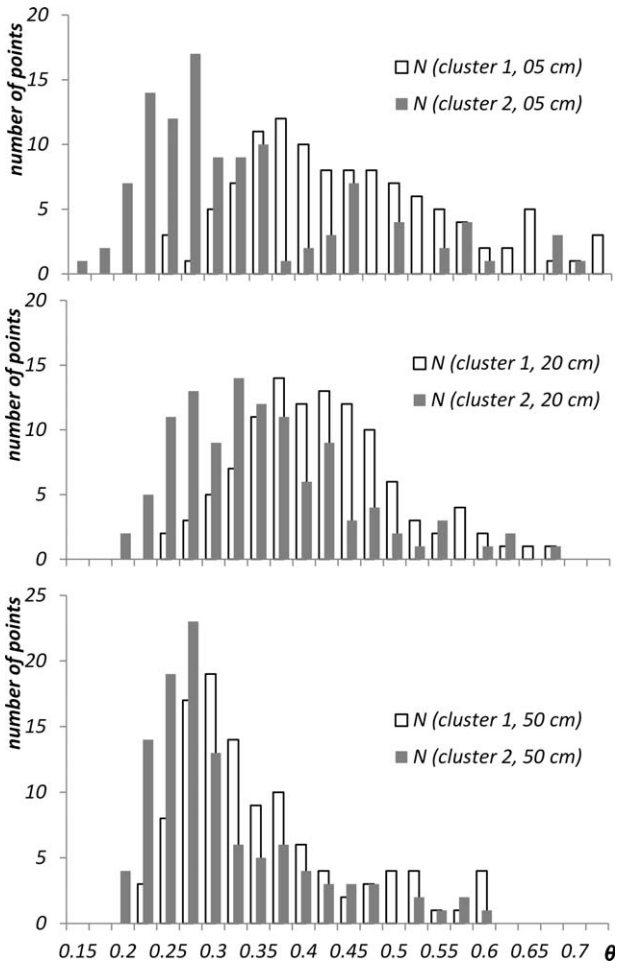

Figure 11. Soil water content histograms (class width 0.025) of the "wet" cluster 1 and the "dry" cluster 2 for different soil depths.

finding agrees well with a conceptual overview on the relation between the temporal mean and variance of soil water content along a hillslope by *Verhoest et al.* [1998, Figure 1]. The "wet" cluster had an approximately unimodal probability density distribution, whereas the "dry" cluster histogram contains one major group of reduced water content and one (50 cm) or several (5 cm) smaller groups of points remaining close to saturation. Hypothetically, the different small groups at the 5 cm level differ in porosity.

Together with the times series of soil water content, Figure 2 also indicates the prevailing cluster. The "dry" pattern of cluster 2 dominated in summer, but the length of this time period varied strongly between years. The change between both patterns occurred at mean soil water content of about 0.35 cm^3/cm^3. A slight hysteresis effect can be observed, with the onset of cluster 2 during rewetting phases occurring at higher soil water content than the onset of cluster 1 during drying phases. This effect might contribute to the observation that both patterns typically tend to remain stable for prolonged periods in spite of short-term fluctuations of mean soil water content. Note that with independent methods based on stable isotope measurements, M. P. Stockinger et al. (Seasonal soil moisture patterns control transit time distributions in a forested headwater catchment, submitted to *Water Resources Research*, 2013) found a similar binary tendency of the catchment's hydrological regime, which switches roughly at the same points in time where both studies overlap. Similarly, *Grayson et al.* [1997] assumed that catchments tend to switch between a "wet" pattern dominated by lateral water movement and a "dry" pattern dominated by more local effects.

Since the proximity of the actual soil water content pattern to either cluster 1 or cluster 2 is most unambiguously described by the loading time series of EOF2, a wavelet coherence analysis of the approximately linear relation between this loading and mean soil water content, which was already presented as a global scatterplot in Figure 9, can help to identify regions in the frequency and time domain where the close relation between the spatial average and the pattern of soil water content breaks down (Figure 12).

The only major breakdown in the otherwise close relation for the soil water content at 5 cm happened in spring 2011 and was limited to short and intermediate time scales below 3 months. During this period also SWC at 50 cm showed lowest correlation. This was the most prolonged drying phase within the study period (Figure 2), which is in agreement with the indications of water limitation found in section 4.1. Due to the absence of short-term fluctuations in soil water content during this time, little or no coherence could be found at time scales shorter than the length of the drying period. Near its end, soil water content also reached the lower end of its range, where no linear relation to the loading of EOF2 was to be expected any more according to Figure 9. The phase angles reveal a slight tendency of the pattern loading to lag behind mean soil water content in those

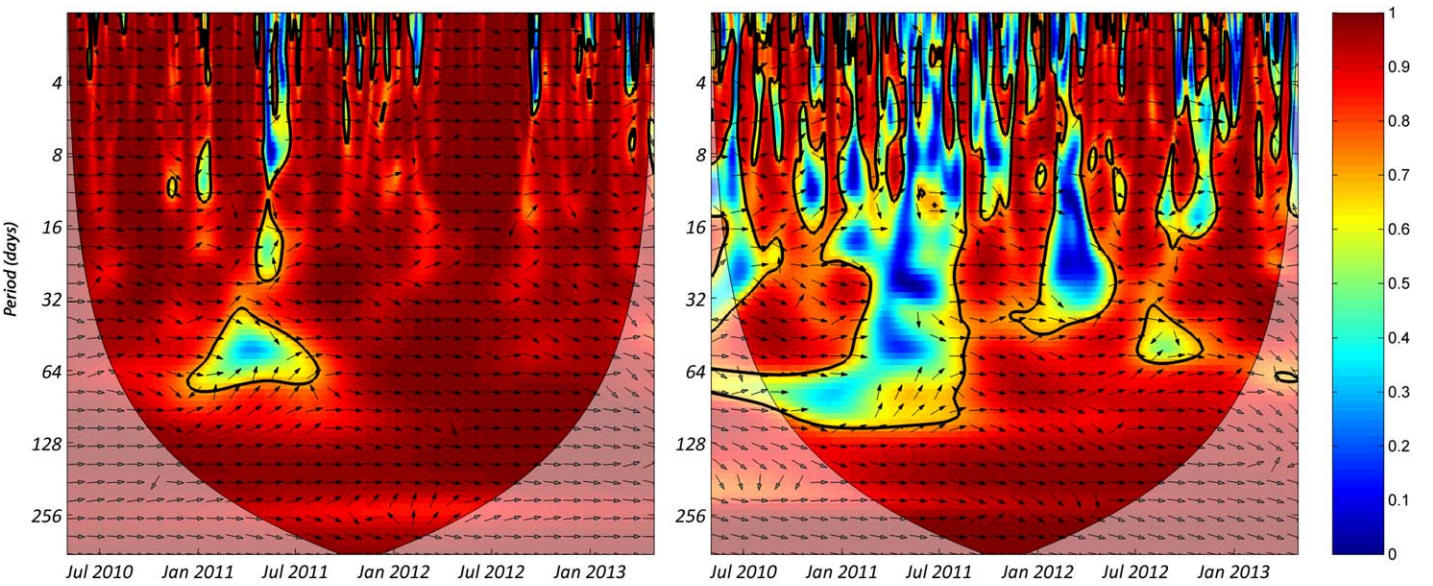

Figure 12. Same as Figures 4 and 7, but for the loading of EOF2 versus horizontally averaged soil water content at the (left) 5 cm and (right) 50 cm level.

regions where coherence is strongest, but varied considerably between regions of weaker coherence, making it difficult to gain deeper insight into possible hysteresis effects by wavelet analysis alone.

We therefore picked four consecutive subperiods representing drying and wetting on different levels, which are highlighted in another version of Figure 9 (Figure 13, similar to *Rosenbaum et al.* [2012] which was based on the same data source, but a shorter then available study period not including the long drying phase in spring 2011).

In agreement with earlier findings [*Rosenbaum et al.*, 2012; *Vivoni et al.*, 2010], spatial variance in the intermediate water content range was higher during a long wetting (autumn 2011, blue) than during a long drying event (spring 2011, red). However, this was not caused by a difference in the slope of the relation between these events themselves, but by an offset built up during summer 2011, which was characterized by a long series of rapidly interchanging low-amplitude wetting and drying events and no net change in water content (gray). The importance of EOF 1 and 2, in contrast, was subject to a clear hysteresis between drying and wetting events themselves. In agreement with the onset of cluster-based pattern changes shown in Figure 2, this hysteresis was such that the typical loading combination of the "dry" pattern resisted quick changes by rewetting. While the (gray) period of interchanging small drying and wetting events in summer 2011 increased variance, it had a restoring effect on the pattern, shifting the loadings of both EOFs back toward their state during drying. One possible hypothesis that could be derived from Figure 13 is that the expression of the spatial pattern is an inert process, which cannot keep pace with fast changes of the spatial mean water content.

Another explanation would be that the effect of drainage-dominated drying on the spatial pattern and variance is different from the effect of evapotranspiration-dominated drying. Most of the spring 2011 (red) drying phase in Figure 13, starting from about 0.37 cm^3/cm^3 downward, can be attributed to evapotranspiration: During this period, potential evapotranspiration was at its maximum and runoff near its minimum (Figure 2). All other drying events shown in Figure 13 represent various degrees of a less evapotranspiration and more drainage-dominated drying. Compared to the extreme case of evapotranspiration-dominated drying, they caused less reduction of variance (below 0.34 cm^3/cm^3), less decline in the contrast of EOF 1 (below 0.34 cm^3/cm^3), and a less rapid change of the loading of EOF 2 toward the "dry" state (at least below 0.39 cm^3/cm^3). *Albertson and Montaldo* [2003] argued that if transpiration is limited by soil water content, the spatial covariance of both variables becomes negative and transpiration will decrease the spatial variance. It was demonstrated above that in our study catchment, water limitation is generally rare and weak, with exception of the spring 2011 drying phase. The stronger decline in variance during this period

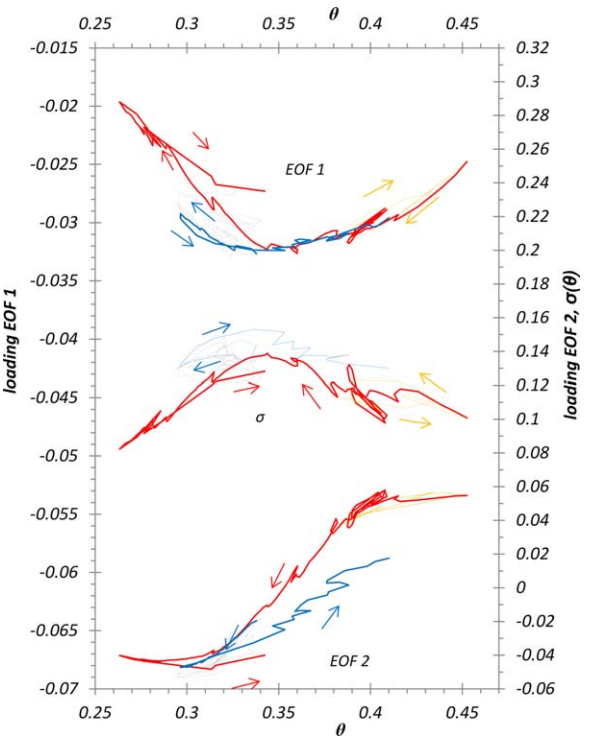

Figure 13. Same as Figure 9, but only for four consecutive subperiods, highlighted as colored lines. The shown period starts 13 November 2010 with a drying-wetting cycle on a high water content level (yellow), followed by a long spring drying phase from the global maximum to the global minimum of the study period and a moderate rewetting (red), a series of short dry-wet cycles in summer 2011 (gray) and the last drying phase of autumn followed by a strong rewetting event, ending with a maximum at 24 December 2011. The subperiods can be compared to the temporal evolution of mean water content in Figure 2.

compared to shorter drying periods might therefore support the theory of variance consumption by water-limited (evapo)transpiration.

5. Conclusions

We measured all major water budget components in or near a small forested catchment over three consecutive years and analyzed them with respect to four research questions (section 1).

1. The water balance on time scales of 1 year or longer closed extremely well; residuals for each year and particularly for the whole study period (2% of precipitation) were smaller than the expected uncertainties of the measurements and might therefore in part be incidental (section 4.1).

2. On a daily time scale, the residual was correlated to horizontal averages of distributed soil water content measurements at three depths, particularly to the deepest measurement level at 50 cm. Only after aggregating from daily to weekly resolution, however, soil water content explained more than half of the residual variance; we attribute this effect to unaccounted fast-turnover storage turns such as interception. The actual time scale at which this effect levels out, as well as another decorrelation source in winter hypothetically attributed to snowpacks, were revealed by the wavelet analysis. The coefficients of a multiple linear regression match well with a weighing rule for estimating the soil water storage term from the three levels based on geometrical considerations (section 4.2).

3. We found that the spatiotemporal dynamics of the soil water storage term are due to pattern variations beyond mere variations of the spatial average and standard deviation parameters of a single pattern. EOF analysis enabled the description of this variability by two underlying patterns and their time-variant weights. Most of this pattern variability was still systematically related to the spatial average of soil water content. Some intricacies in the relation between space-average soil water content and its spatial pattern could be attributed to hysteresis effects and differences in the effect of drainage-dominated versus evapotranspiration-dominated drying (section 4.3). Evapotranspiration accounted for less than half of precipitation and was mostly energy limited. The European drought in spring 2011, which severely affected agriculture in a contiguous area surrounding our study site [*Sepulcre-Canto et al.*, 2012], had a marginal effect on sums and ratios in the annual water budget of that year (see section 4.1, particularly Table 2 and Figure 3). But its impact on the coherence between actual and potential evapotranspiration, between their ratio and soil water content, and on the spatial pattern of soil water content could be observed until autumn 2011 with wavelet analysis (see sections 3.2 and 3.3). Our methodological framework of wavelet coherence and EOF analysis enabled the investigation of the large data set for time scales, time periods, and patterns relevant to our research questions, without making prior assumptions on their identity and being only restricted to linearity assumptions. The identification of scales and patterns using these methods minimizes the risk of overlooking unexpected processes. Once these scales are identified, wavelet and EOF

methods can often be replaced by simpler methods such as temporal aggregation (section 4.2) or by using space-averaged water content as a proxy for the dominating pattern (section 4.3).

Acknowledgments
This work was supported by the German Science Foundation (DFG) Transregional Collaborative Research Centre SFB/TR32: Patterns in Soil-Vegetation-Atmosphere-Systems and the Helmholtz Society initiative TERENO (Terrestrial Environmental Observatories). We thank Dirk Hoffmeister (University of Köln, TR32 subproject Z1) and the German Weather Service DWD for providing precipitation data. These data can be purchased from the DWD (Deutscher Wetterdienst), for all other data contact the corresponding author. This study would not have been possible without the assistance of numerous volunteers and technicians in setting up and maintaining the wireless soil water content network, the flux tower, the climate station, and the runoff gauge, especially Ansgar Weuthen, Bernd Schilling, Ferdinand Engels, Normen Hermes, Ulrike Rosenbaum (Forschungszentrum Jülich), Raimar Schlenkhuhn, and Uwe Baltes (University of Trier). Substantial parts of the footprint model implementation used were coded by Anneke van de Boer, Wageningen University. The fundamental steps of the wavelet analysis were performed with a software package provided by A. Grinsted, National Oceanography Centre of the United Kingdom including functions provided by C. Torrence, National Center for Atmospheric Research of the U.S.A. and G. Compo, University of Colorado at Boulder, USA. Two anonymous reviewers and the associate editor provided valuable suggestions improving the clarity and completeness of the manuscript.

References

Albertson, J. D., and N. Montaldo (2003), Temporal dynamics of soil moisture variability: 1. Theoretical basis, *Water Resour. Res.*, *39*(10), 1274, doi:10.1029/2002WR001616.

Allen, R. G., L. S. Pereira, D. Raes, and M. Smith (1998), Crop evapotranspiration: Guidelines for computing crop water requirements, *Food and Agric. Organ. of the U. N. Irrig. Drain. Pap. 56*, 300 pp, FAO, Rome, Italy.

Bogena, H., et al. (2012), TERENO - Ein langfristiges Beobachtungsnetzwerk für die terrestrische Umweltforschung, *Hydrol. Wasserbewirtschaftung*, *3*, 138–143.

Bogena, H. R., J. A. Huisman, C. Oberdörster, and H. Vereecken (2007), Evaluation of a low-cost soil water content sensor, *J. Hydrol.*, *344*, 32–42, doi:10.1016/j.jhydrol.2007.06.032.

Bogena, H. R., M. Herbst, J. A. Huisman, U. Rosenbaum, A. Weuthen, and H. Vereecken (2010), Potential of wireless sensor networks for measuring soil water content variability, *Vadose Zone J.*, *9*, 1002–1013, doi:10.2136/vzj2009.0173.

Bogena, H. R., et al. (2014), A terrestrial observatory approach for the integrated investigation of the effects of deforestation on water, energy, and matter fluxes, *Sci. China Earth Sci.*, doi:10.1007/s11430-014-4911-7, in press.

Budyko, M. I. (1974), *Climate and Life*, 508 pp., Academic, N. Y.

Chen, B., T. A. Black, N. C. Coops, T. Hilker, J. A. Trofymow, and K. Morgenstern (2009), Assessing tower flux footprint climatology and scaling between remotely sensed and eddy covariance measurements, *Boundary Layer Meteorol.*, *130*, 137–167, doi:10.1007/s10546-008-9339-1.

Cornelissen, T., B. Diekkrüger, and H. R. Bogena (2014), Significance of scale and lower boundary condition in the 3D simulation of hydrological processes and soil moisture variability in a forested headwater catchment, *J. Hydrol.*, doi:10.1016/j.hydrol.2014.01.060, in press.

Drüe, C., A. Graf, G. Heinemann, and T. Pütz (2012), Observation of atmosphere-forest exchange processes at the new TERENO site Wüstebach, paper presented at 20th Symposium on Boundary Layers and Turbulence, Boston, Mass, 9–13 Jul, AMS (American Meteorological Society).

Etmann, M. (2009), Dendrologische Aufnahmen im Wassereinzugsgebiet Oberer Wüstebach anhand verschiedener Mess- und Schätzverfahren, Master thesis, Univ. of Münster, Münster, Germany.

Foken, T., M. Aubinet, J. J. Finnigan, M. Y. Leclerc, M. Mauder, and K. T. Paw U (2011), Results of a panel discussion about the energy balance closure correction, *Bull. Am. Meteorol. Soc.*, *92*, ES13–ES18, doi:10.1175/2011BAMS3130.1.

Graf, A., et al. (2011), Temporal downscaling of soil carbon dioxide efflux measurements based on time-stable spatial patterns, *Vadose Zone J.*, *10*, 239–251, doi:10.2136/vzj2009.0152.

Graf, A., M. Herbst, L. Weihermüller, J. A. Husiman, N. Prolingheuer, L. Bornemann, and H. Vereecken (2012), Analyzing spatiotemporal variability of heterotrophic soil respiration at the field scale using orthogonal functions, *Geoderma*, *181–182*, 91–101, doi:10.1016/j.geoderma.2012.02.016.

Grayson, R. B., A. W. Western, F. H. S. Chiew, and G. Blöschl (1997), Preferred states in spatial soil moisture patterns: Local and nonlocal controls, *Water Resour. Res.*, *33*, 2897–2908.

Grinsted, A., J. C. Moore, and S. Jevrejeva (2004), Application of the cross wavelet transform and wavelet coherence to geophysical time series, *Nonlinear Processes Geophys.*, *11*, 561–566, doi:10.5194/npg-11-561-2004.

HK100 (2009), *Hydrogeological Map of North Rhine-Westphalia (1:100 000)*, Geol. Surv. North Rhine-Westphalia, Krefeld, Germany.

Högström, U., and I. Larsson (1968), Studies on the water balance of a small natural catchment area in southern Sweden, *Tellus*, *20*, 633–641.

Hsieh, C., G. Katul, and T. Chi (2000), An approximate analytical model for footprint estimation of scalar fluxes in thermally stratified atmospheric flows, *Adv. Water Resour.*, *23*, 765–772.

Hu, W., and B. C. Si (2013), Soil water prediction based on its scale-specific control using multivariate empirical mode decomposition, *Geoderma*, *193–194*, 190–188, doi:10.1016/j.geoderma.2012.10.021.

Hu, W., and B. C. Si (2014), Can soil water measurements at a certain depth be used to estimate mean soil water content of a soil profile at a point or at hillslope scale?, *J. Hydrol.*, doi:10.1016/j.hydrol.2014.01.053, in press.

Kampf, S. K., and S. J. Burges (2010), Quantifying the water balance in a planar hillslope plot: Effects of measurement errors on flow prediction, *J. Hydrol.*, *380*, 191–202.

Kang, S., and H. Lin (2007), Wavelet analysis of hydrological and water quality signals in an agricultural watershed, *J. Hydrol.*, *338*, 1–14.

Koch, R., J. Rudi, G. Jager, R. Pabel, H. Bogena, and A. Kunoth (2010), Multiscale analysis of hydrologic time series data using the Hilbert-Huang-Transform (HHT), *Vadose Zone J.*, *9*, 925–942, doi:10.2136/vzj2009.0163.

Kormann, R., and F. X. Meixner (2001), An analytical footprint model for non-neutral stratification, *Boundary Layer Meteorol.*, *99*, 207–224.

Korres, W., C. Koyama, P. Fiener, and K. Schneider (2010), Analysis of surface soil moisture patterns in agricultural landscapes using empirical orthogonal functions, *Hydrol. Earth Syst. Sci.*, *14*, 751–764, doi:10.5194/hess-14-751-2010.

Lauzon, N., F. Anctil, and J. Petrinovic (2004), Characterization of soil moisture conditions at temporal scales from a few days to annual, *Hydrol. Processes*, *18*, 3235–3254, doi:10.1002/hyp.5656.

Mauder, M., R. L. Desjardins, S. P. Oncley, and I. MacPherson (2007), Atmospheric response to a partial solar eclipse over a cotton field in central California, *J. Appl. Meteorol. Climatol.*, *46*, 1792–1803, doi:10.1175/2007JAMC1495.1.

Mauder, M., M. Cuntz, C. Drüe, A. Graf, C. Rebmann, H. P. Schmid, M. Schmidt, and R. Steinbrecher (2013), A strategy for quality and uncertainty assessment of long-term eddy-covariance measurements, *Agric. For. Meteorol.*, *169*, 122–135, doi:10.1016/j.agrformet.2012.09.006.

Mittelbach, H., and S. I. Seneviratne (2012), A new perspective on the spatio-temporal variability of soil moisture: Temporal dynamics versus time-invariant contributions, *Hydrol. Earth Syst. Sci.*, *16*, 2169–2179, doi:10.5194/hess-16-2169-2012.

Moffat, A. M., et al. (2007), Comprehensive comparison of gap-filling techniques for eddy covariance net carbon fluxes, *Agric. For. Meteorol.*, *147*, 209–232, doi:10.1016/j.agrformet.2007.08.011.

Parent, A.-C., F. Anctil, and L.-E. Parent (2006), Characterization of temporal variability in near-surface soil moisture at scales from 1 h to 2 weeks, *J. Hydrol.*, *325*, 56–66, doi:10.1016/j.jhydrol.2005.09.027.

Peres-Neto, P., D. A. Jackson, and K. M. Somers (2005), How many principal components? Stopping rules for determining the number of non-trivial axes revisited, *Comput. Stat. Data Anal.*, *49*, 974–997, doi:10.1016/j.csda.2004.06.015.

Perry, M. A., and J. D. Niemann (2007), Analysis and estimation of soil moisture at the catchment scale using EOFs, *J. Hydrol.*, *334*, 388–404, doi:10.1016/j.jhydrol.2006.10.014.
Perry, M. A., and J. D. Niemann (2008), Generation of soil moisture patterns at the catchment scale by EOF interpolation, *Hydrol. Earth Syst. Sci.*, *12*, 39–53.
Pütz, T., R. Kiese, S. Zacharias, H. Bogena, E. Priesack, U. Wollschläger, M. Schwank, H. Papen, G. v. Unold, and H. Vereecken (2011), TERENO-SOILCan - Ein Lysimeter Netzwerk in Deutschland [in German], paper presented at 14th Gumpensteiner Lysimetertagung Gumpenstein., LRG (Lysimeter Research Group), Raumberg-Gumpenstein, Austria.
Richter, D. (1995), Ergebnisse methodischer Untersuchungen zur Korrektur des systematische Meßfehlers des Hellmann-Niederschlagmessers, in *Berichte des Deutschen Wetterdienstes*, vol. 194, 93 pp, LRG (Lysimeter Research Group), Selbstverlag des Deutschen Wetterdienstes, Offenbach am Main, Germany.
Rosenbaum, U., H. R. Bogena, M. Herbst, J. A. Huisman, T. J. Peterson, A. Weuthen, A. W. Western, and H. Vereecken (2012), Seasonal and event dynamics of spatial soil moisture patterns at the small catchment scale, *Water Resour. Res.*, *48*, W10544, doi:10.1029/2011WR011518.
Rutter, A. J., and A. J. Morton (1977), A predictive model of rainfall interception in forests: III. Sensitivity of the model to stand parameters and meteorological variables, *J. Appl. Ecol.*, *14*, 567–588.
Schaefli, B., and E. Zehe (2009), Hydrological model performance and parameter estimation in the wavelet-domain, *Hydrol. Earth Syst. Sci.*, *13*, 1921–1936.
Sepulcre-Canto, G., S. Horion, A. Singleton, H. Carrao, and J. Vogt (2012), Development of a combined drought indicator to detect agricultural drought in Europe, *Nat. Hazards Earth Syst. Sci.*, *12*, 3519–3531, doi:10.5194/nhess-12-3519-2012.
Si, B. C. (2008), Spatial scaling analyses of soil physical properties: A review of spectral and wavelet methods, *Vadose Zone J.*, *7*, 547–562, doi:10.2136/vzj2007.0040.
Torrence, C., and G. P. Compo (1998), A practical guide to wavelet analysis, *Bull. Am. Meteorol. Soc.*, *79*, 61–78, doi:10.1175/1520-0477(1998)079<0061:APGTWA>2.0.CO;2.
Tromp-van Meerveld, H. J., and J. J. McDonnell (2006), Threshold relations in subsurface stormflow: 2. The fill and spill hypothesis, *Water Resour. Res.*, *42*, W02411, doi:10.1029/2004WR003800.
van de Boer, A., A. F. Moene, D. Schüttemeyer, and A. Graf (2013), Sensitivity and uncertainty of analytical footprint models according to a combined natural tracer and ensemble approach, *Agric. For. Meteorol.*, *169*, 1–11, doi:10.1016/j.agrformet.2012.09.016.
van Dijk, A., A. F. Moene, and H. A. R. de Bruin (2004), The principle of surface flux physics: Theory, practice and description of the ECPACK library, *Internal Rep. 2004/1*, 99 pp., Meteorol. and Air Qual. Group, Wageningen Univ., Wageningen, Netherlands.
Vargas, R., M. Detto, D. Baldocchi, and M. F. Allen (2010), Multiscale analysis of temporal variability of soil CO2 production as influenced by weather and vegetation, *Global Change Biol.*, *16*, 1589–1605, doi:10.1111/j.1365-2486.2009.02111.x.
Vereecken, H., T. Kamai, T. Harter, R. Kasteel, J. Hopmans, and J. Vanderborght (2007), Explaining soil moisture variability as a function of mean soil moisture, a stochastic unsaturated flow perspective, *Geophys. Res. Lett.*, *34*, L22402, doi:10.1029/2007GL031813.
Verhoest, N. E. C., P. A. Troch, C. Paniconi, and F. P. de Troch (1998), Mapping basin scale variable source areas from multitemporal remotely sensed observations of soil moisture behavior, *Water Resour. Res.*, *34*, 3235–3244.
Vivoni, E. R., J. C. Rodríguez, and C. J. Watts (2010), On the spatiotemporal variability of soil moisture and evapotranspiration in a mountainous basin within the North American monsoon region, *Water Resour. Res.*, *44*, W00D06, doi:10.1029/2008WR008240.
Webster, R. (1997), Regression and functional relations, *Eur. J. Soil Sci.*, *48*, 557–566.
Western, A. W., R. B. Grayson, and G. Blöschl (2002), Scaling of soil moisture: A hydrological perspective, *Annu. Rev. Earth Planet. Sci.*, *30*, 149–180, doi:10.1146/annurev.earth.30.091201.140434.
Williams, C. A., et al. (2012), Climate and vegetation controls on the surface water balance: Synthesis of evapotranspiration measured across a global network of flux towers, *Water Resour. Res.*, *48*, W06523, doi:10.1029/2011WR011586.
Wilson, K. B., P. J. Hanson, P. J. Mulholland, D. D. Baldocchi, and S. D. Wullschleger (2001), A comparison of methods for determining forest evapotranspiration and its components: Sap-flow, soil water budget, eddy covariance and catchment water balance, *Agric. For. Meteorol.*, *106*, 153–168, doi:10.1016/S0168–1923(00)00199-4.
Yoo, C., and S. Kim (2004), EOF analysis of surface soil moisture field variability, *Adv. Water Resour.*, *27*, 831–842, doi:10.1016/j.advwatres.2004.04.003.
Zacharias, S., et al. (2011), A network of terrestrial environmental observatories in Germany, *Vadose Zone J.*, *10*, 955–973, doi:10.2136/vzj2010.0139.